# Comparative Analysis in Drilling Performance of AA7075 in Different Temper Conditions

**ESER YARAR** ( e.yarar@hotmail.com )
Kocaeli Üniversitesi https://orcid.org/0000-0003-1187-5382
**Alpay Tamer ERTURK**
Kocaeli University
**Funda Gül KOÇ**
Kocaeli University
**Fahri VATANSEVER**
Kocaeli University

**Research Article**

**Keywords:** AA7075, temper condition, drilling, response surface methodology, finite element method

**Posted Date:** May 23rd, 2022

**DOI:** https://doi.org/10.21203/rs.3.rs-633600/v2

**Comparative Analysis in Drilling Performance of AA7075 in Different Temper Conditions**

Eser YARAR[a,*], A. Tamer ERTURK[a], Funda Gül KOÇ[b], Fahri VATANSEVER[a]

[a]*Department of Mechanical Engineering, Kocaeli University, Kocaeli, Turkey*
[b]*Department of Metallurgical and Materials Engineering, Kocaeli University, Kocaeli, Turkey*

*Corresponding author: eser.yarar@kocaeli.edu.tr e.yarar@kocaeli.edu.tr

**A B S T R A C T**

The main objective of this study is to examine the machinability and the surface quality conditions of the AA7075 material with different temper conditions. For this purpose, various temper treatments are implemented to evaluate the impact of microstructural properties on tool wear and the surface quality of the drilled holes. The drilling operations have been done on 0, F, T4, T6, and T7 temper conditions. Process parameters were three different spindle speeds (715, 1520, and 3030 rev/min) and three feed rates (0.1, 0.2, and 0.3 mm/rev) with HSS-G high-performance ground standard twist drill bit. The present work deals with the effects of temper conditions on thrust force, drilling temperature, tool wear, surface integrity, and chip morphology. Response surface methodology was used in the evaluation of experiment results. The optimization results showed that while thrust force and torque are not significantly affected by a change in spindle speed, they are sensitive to an increase in feed rate. Heat-generation on the drill bit is the lowest at low levels of both the feed rate and spindle speed parameters. The AA7075-T6 condition specimen was machined with continuous chip formation, resulting in the best hole surface quality. The 3D finite element modeling of the drilling process was carried out, and the drilling performance of AA7075-T6 was evaluated in terms of thrust force, heat generation, and chip formation.

***Keywords:*** AA7075, temper condition, drilling, response surface methodology, finite element method

**GRAPHICAL ABSTRACT**

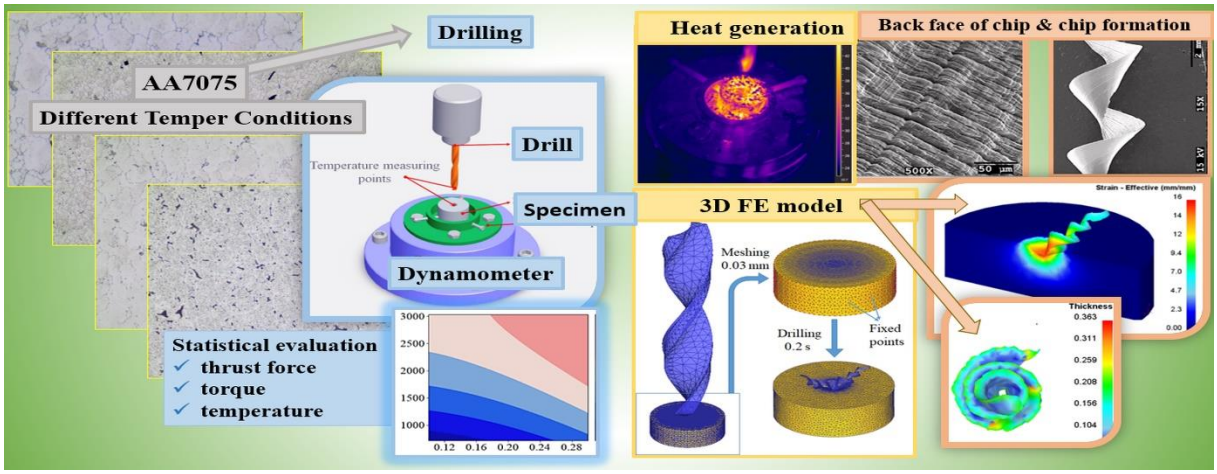


## 1. Introduction

7xxx series with chromium alloying elements are replacing many structural parts due to their stress corrosion cracking (SCC) tendency of other aluminum alloys [1]. These alloys are classified as a precipitation-hardened alloy type by an obstacle to the dislocation movements of small and homogeneously dispersed precipitates [2]. A heat-treatment process reconfigures the

crystal structure to strengthen the mechanical properties of alloys. Generally, the heat treatments applied to AA7075 are T4, T6, and T7 by their usage area. T4 is defined as natural aging, while T6 and T7 are classified as artificial aging. On the other hand, SCC sensitivity may increase when these alloys are tempered especially to the highest strength. SCC is a dangerous type of corrosion and can cause sudden damage even under mechanical loading conditions that are well below the tensile strength of the materials [3]. AA7075 (Al-Zn-Mg-Cu) is used in aircraft, aerospace, automobile, and transportation industries to make durable and lightweight structural components [4–6]. T6 heat treated alloys are mainly consist of finely and densely distributed GP zones and η precipitates within grains and continuous precipitates along the grain boundaries. Thus, the alloys obtain the highest hardness and strength with T6 heat treatment. The precipitates become coarser and discontinuous in grain boundaries and grains with T7 over aging heat treatment [7]. Surface integrity is critical to fatigue failure, especially in an application in the aerospace industry [8], as drilling causes microcracks on the hole surface that weaken the material against fatigue damage. The main properties of metallic materials which affect machinability are hardness, ductility, and toughness. Zn and Mg alloying elements present in the AA7075 produce the $MgZn_2$ intermetallic phase resulting in an aging treatment, which causes an increase in the strength. Aluminum alloys are comparatively soft materials having specific problems in drilling [5,9].

The hard intermetallic in the aluminum alloy and the sticking tendency due to the soft structure of the aluminum matrix have a significant effect on the tool life more than expected in the drilling process [10]. The temperature during the drilling operation is a limiting factor of machining because that tool life decreases with higher temperatures [11]. In addition, since the temperature increase affects the main mechanical properties of the material due to the complex thermo-mechanical interaction between the tools and the workpiece, such as elasticity and plasticity, the hole surface quality is also indirectly affected [12,13]. Surface microcracks caused by the cutting mechanism are the main reason why roughness and fatigue life effects in machining during drilling [14]. The main parameters affecting the surface quality in drilling are spindle speed, feed rate, the inclination of the tool with the drilled surface, and feed direction. Studies without statistical methods are unsuccessful in determining which parameter has a significant impact on performance characteristics, and it requires a lot of experimentation and data [15]. Therefore, several papers have been published on the optimization of cutting parameters in machining. For example, Sofuoğlu et al. applied multi-objective optimization based on input parameters using hybrid decision-making for the machining process [16]. In another study, Arapoğlu et al. used artificial neural networks for surface roughness prediction [17], and in another study, Orak et al. used an ANN-based decision-making method to determine the optimum processing parameters [18]. Similarly, Gök et al. investigated the effect of the cutting tool material on chatter vibrations in the machining of AA7075 by using regression analysis [19]. Çakıroğlu and Acır investigated drill bit temperature in the drilling process of Al 7075 alloys by using the Taguchi design method and they found that the most significant factor in affecting the drill temperature ise feed rate [20]. Rajeswari and Amirthagadeswaran studied multiresponse optimization of end milling in aluminum composites using Response Surface Methodology (RSM) based grey relational analysis [21]. According to their findings, spindle speed and weight percentage of SiC are the most significant factors affecting the machinability of hybrid composites. Nripen Mondal *et al.* performed regression analysis with satisfactory accuracy for finding optimal conditions in an aluminum alloy drilling [22]. According to their study, burr height increases with increasing feed rate. In these studies, the target material properties were kept constant, and it was aimed to optimize the machining process by changing the cutting parameters or cutting tool properties. Some extra information allows researchers to obtain from a few recent studies on the microstructures encountered with

various aging processes for the AA7075 alloy [23–26]. There are different studies for AA7075-O in the literature. However, research for the other temper conditions is limited [5,27]. Within the scope of this study, heat treatments used in general industrial applications were performed, and microstructures were discussed. The properties of drilling parameters on chip formation were investigated when drilling AA7075 test samples. RSM is one of the powerful optimization tools frequently used in experimental research in recent years for statistical evaluation. This study reports optimize the multiple performance characteristics for different temper conditions in the dry drilling of AA7075. Heat generation detrimentally affects hole quality. Thus, the temperature and the surface roughness were measured and analyzed during drilling for each alloy condition. For practical considerations, this article will shed light on the decision at which stage of production the drilling operation should be performed. Based on the findings presented, manufacturing engineers can decide whether to drill before or after heat treatment application. The finite element method (FEM) was used to comparison and verification test data.

## 2. Material and Method

### 2.1. Heat-treatment and microstructural characterization

In this study, the effect of various heat treatment applications on the machinability properties of AA7075 series aluminum alloy was investigated. For this purpose, different heat-treatments were applied to the extruded AA7075 specimens with a dimension of Ø25 mm. Table 1 shows the chemical composition of the AA7075 used in this study. Different heat-treatment processes performed on the test specimens are given in Table 2. Mechanical properties of AA7075 according to different temper conditions are given in Table 3. Due to temperature differences, 7075 alloys show different mechanical strength behavior as presented in Table 3. The 0-condition exhibits ductile behavior with the lowest tensile strength and highest elongation. 7075-T6 alloy shows the highest tensile strength but the lowest elongation property.

**Table 1.** The chemical composition of the investigated AA7075 (wt.%).

| | Si | Fe | Cu | Mn | Mg | Zn | Cr | Ti | Al |
|---|---|---|---|---|---|---|---|---|---|
| This study | 0.10 | 0.22 | 1.70 | 0.09 | 2.51 | 5.75 | 0.18 | 0.02 | Bal. |
| EN 573-3 | ≤0.40 | ≤0.50 | 1.2-2.0 | ≤0.30 | 2.1-2.9 | 5.1-6.1 | 0.18-0.28 | ≤0.20 | |

**Table 2.** Different heat treatment processes applied to specimens in the study.

| Temper | Process parameters of the heat-treatment | Hardness (HV3) |
|---|---|---|
| 0 | Annealed, the lowest strength, highest ductility temper, 415 °C for 3 h, cooling in the furnace. | 65 ± 0.78 |
| F | As fabricated, extrusion rod supplied from the market in T6 condition | 190± 1.54 |
| T4 | Solution treatment at 480 °C for 3 h, quenching in water at room temperature and natural aging for 72 h. | 142.70 ± 1.98 |
| T6 | Solution treatment at 480 °C for 3 h, quenching in water at room temperature and artificial aging at 120 °C for 24 h. | 188.46 ± 0.73 |
| T7 | Solution treatment at 480 °C for 3 h, quenching in water at room temperature and artificial over aging at 165 °C for 24 h. | 165.82 ± 2.17 |

**Table 3.** The mechanical properties of different AA7075 [28,29]

| Temper | Ultimate Tensile Strength (MPa) | Tensile Yield Strength (MPa) | Elongation (%) |
|---|---|---|---|
| **0** | 230 | 105 | 17 |
| **T4** | 396.8 | 250.9 | 15 |

| | | | |
|---|---|---|---|
| **T6** | 570 | 505 | 11 |
| **T7** | 505 | 435 | 13 |

Microstructural investigations were performed using an optical microscope (OM) and a Jeol JSM 6060 scanning electron microscope (SEM) with energy-dispersive X-ray spectroscopy (EDX) attachment to observe the changes of microstructure properties obtained after heat treatments. For this purpose, specimens were polished and etched with Graff Sergeant's solution for 20 seconds to reveal the microstructure.

Aging conditions have a significant effect on the size, quantity, and distribution of precipitates. During aging treatment, the size and quantity of precipitates increase, initial precipitates are generally coherent, and then becoming semi-coherent, and finally incoherent with the matrix, respectively. The size, distribution, and consistency of precipitates with the matrix have a significant effect on the properties of Al-Zn-Mg-Cu alloys [30–32]. Figure 1 shows the microstructure of the heat-treated specimens in different conditions. In Figure 1a, it is seen that the microstructure obtained for the 0-condition contains quite coarse intermetallic. More homogeneous and fine dispersed $MgZn_2$ (η) precipitates were observed in the microstructure of F and T6 heat-treated specimens given in Figures 1b and d. These precipitates become coarser and non-uniform distributed with T7 heat treatment as seen in Figure 1e. Also, it was seen that the precipitation amount of T4 heat treated specimen is less than F, T6, and T7 heat-treated specimens accordingly. EDX analysis was performed on specimens to determine the chemical compositions of precipitates observed in the microstructural investigations. According to EDX analysis results given in Figure 1 while small-sized precipitates observed in grain and grain boundaries contain Mg and Zn, coarse precipitates contain Cu, Fe, Mn, and Si. $MgZn_2$ is the main precipitate that increases the hardness of AA7075 series aluminum alloy. Coarse $Al_2CuMg$, AlMnFeSi, and $Al_7Cu_2Fe$ precipitates are formed during solidification and cannot be dissolved by solution treatment [33–35].

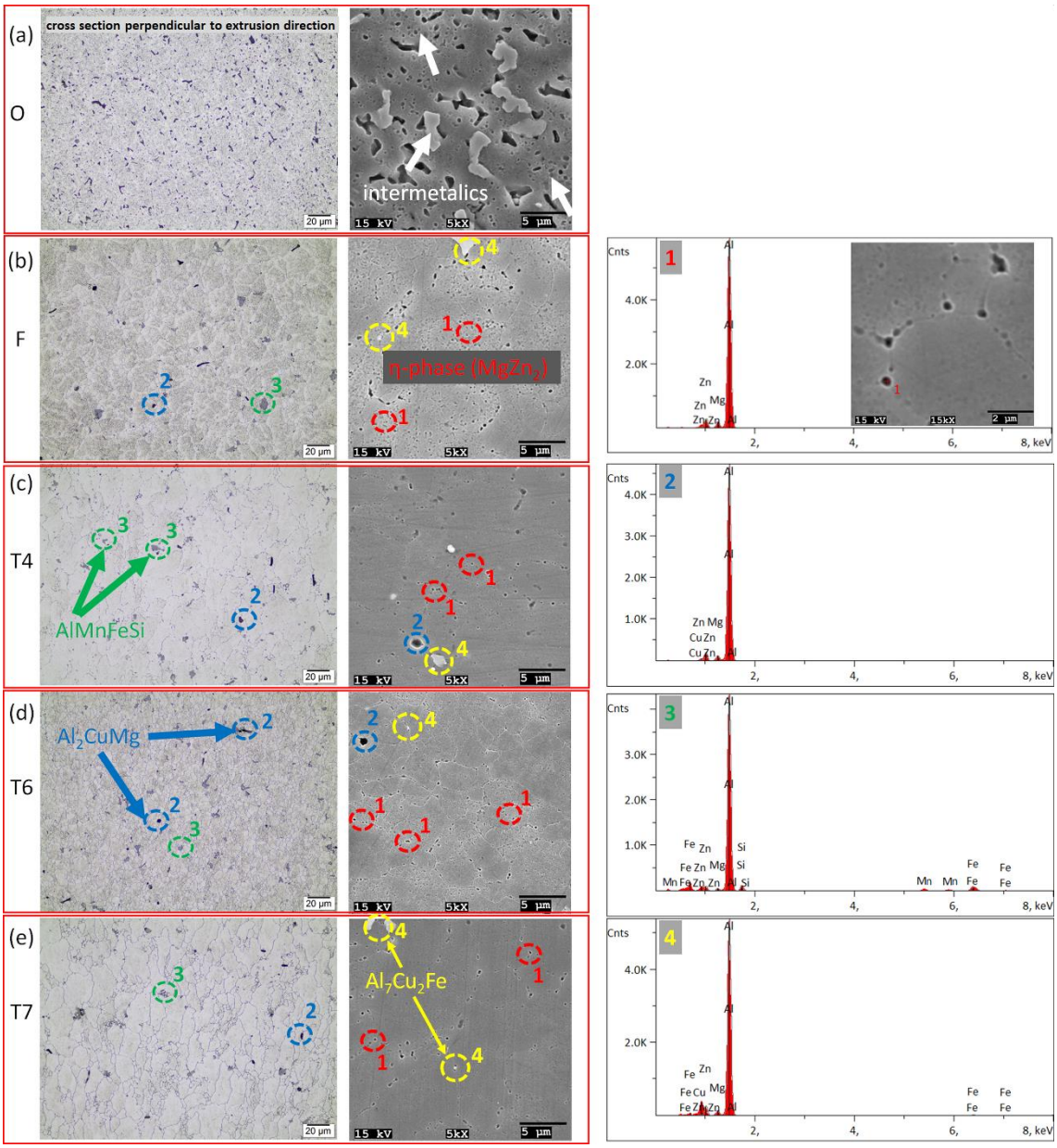


**Figure 1.** Microstructures of the heat-treated specimens.

Hardness tests were applied using a Future-Tech Vickers hardness tester under a 3 kg load for 10 seconds. Five measurements were carried out for each specimen to have an average value. Hardness values of the heat-treated test specimens in different conditions are given in Table 2. High strength and hardness are obtained by reaching the optimum distribution of the fine-sized and high amounts of precipitates. Fine and uniform $MgZn_2$ (η) precipitates coherent with matrix lead to an increase in the hardness and strength of 7075 alloys [35]. Hence, the T6 and F heat-treated specimens show the highest material hardness. The lowest material hardness was obtained in the 0-condition test specimen as expected. Also, it was seen that T4 conditions have a lower hardness value when compared with T6 heat-treated test specimens. This situation shows that more aging time is required to achieve better properties at T4 heat-treatment conditions. It was observed that the hardness of the test specimens decreased as a result of the coarsening in the precipitates due to over-aging with T7 heat treatment.

## 2.2. Experimental set up, optimization and validation procedure

A Toss United TU5032B vertical drill machine was used in the drilling operations. The experimental setup is provided as a schematic overview in Figure 2. A Kistler 9272 piezoelectric dynamometer and a 5070A model amplifier were used for thrust force and torque data collection. A total of 3 samples were prepared for each temper condition, and the thickness of each sample is 10 mm. All drill bits had a nominal diameter of 6 mm. No cutting fluid was used during drilling and all experiments were repeated 3 times. The average surface roughness (Ra) is used to evaluate the surface roughness [36,37]. The surface roughness was measured using 2D Mitutoyo SJ-301 from three different points. The geometric characteristics of each hole have been evaluated with SEM and stereo microscope images. Moreover, chip formations were characterized using thermal images obtained from the infrared camera. Drilling temperatures were recorded with a FLIR-A325sc model infrared camera. The infrared cameras utilize infrared radiation to determine the surface temperature of objects without any physical contact, which is very useful for applications like drilling. The utilization of infrared cameras in drilling operations has been employed, as in early research [37]. The temperature measuring points were 5 mm upper surface of the drill bit and 5 mm lower from the upper surface of the drilled hole. The distance between the thermal camera and temperature measuring points was 50 and 52.5 centimeters for the drill bit and hole surface, respectively. The various aging treatments of 7075 aluminum alloys in drilling were considered and optimized by conducting drilling experiments using Ø6 mm HSS-G high-performance ground standard twist drill, three spindle speeds, three feed rates, as seen in Table 4.

**Table 4.** Selected factors and levels for the DoE model.

| Factors | Levels | Values |
|---|---|---|
| Workpiece material condition | 4 | F, T4, T6, T7 |
| Spindle Speed (rev/min) | 3 | 715; 1520; 3030 |
| Feed Rate (mm/rev) | 3 | 0.1; 0.2; 0.3 |

The full factorial experimental design was employed with the selected parameters [38,39]. RSM is used to statistically evaluate the effect, significance, and interactions of the independent variables, and the optimal dry drilling parameter settings. The purpose of creating a response surface is to estimate the optimum point of this region, which provides particular properties in a design plane consisting of many parameters that are effective on the result in an experimental study. Although the obtained function represents the experimental data, it is all-important that the model fit is high where is necessary to identify the most significant factors with the number of potential effects on one or more responses. By using RSM designs, cause and effect relationships can be expressed with mathematical models, while saving time, resources, and energy. The correctness of the model based on analysis of variance (ANOVA) was revealed, and regression equations were acquired with RSM. The relationship between the independent variables and the responses in RSM is defined by a second-order polynomial model given in Eq. 1.

$$y = \beta_0 + \sum_{i=1}^{k} \beta_i x_i + \sum_{i=1}^{k} \beta_{ii} x_i^2 + \sum_{i=1}^{k-1} \sum_{j=2}^{k} \beta_{ij} X_i X_j + \varepsilon \quad (1)$$

Where $y$ is predicted response, $\beta_0$ is constant, $\beta_i$, $\beta_{ii}$, and $\beta_{ij}$ represent coefficients of linear, quadratic, and interaction terms, respectively. While $X$ shows the coded variables, $\varepsilon$ indicates the error. ANOVA tables, contour, and main effect plots were used in the analysis of the experimental results. ANOVA tables are given in supplementary materials. Test results in the 95% confidence interval for the P values were considered at all variance analyses [39–43].

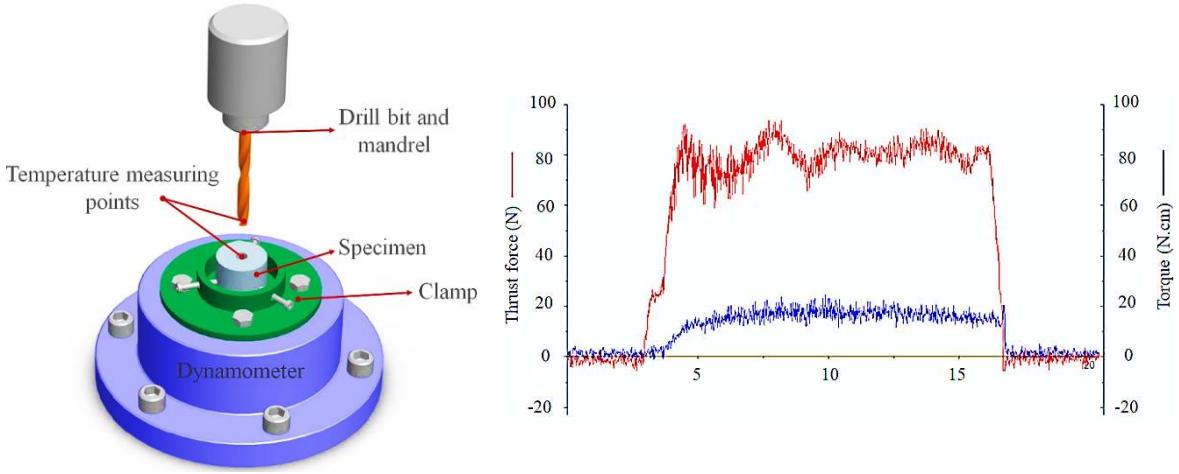


**Figure 2.** Experimental setup of the drilling operations.

## 3. Results

### 3.1. Evaluation of thrust force and torque

The measurement of forces in the drilling system is essential to investigate the effects of workpiece properties. Figures 3 and 4 show the main effect and contour plots for thrust force and torque, respectively. From the main effect plots, both torque ($M_z$) and thrust force ($F_z$) similarly increased by about 93%, with the increased feed rate from 0.1 to 0.3. Contrary to this, the spindle speed increase resulted in a slight decrease in $M_z$ and $F_z$. Among the heat treatment types, the differences in $F_z$ obtained varied by up to 10%. Drilling T6 heat-treated samples resulted in the lowest thrust force value around the mean of 100N. In general, thrust force increases as increasing elongation behavior when considering the test results values with the mechanical properties given in Table 3. In other words, increasing ductility increases the thrust forces during drilling. Similarly, the ductile property of the hardened material tends to decrease due to the increase in strength after heat treatment. As a result, the thrust force and torque generated during drilling tend to lessen with higher strength properties.

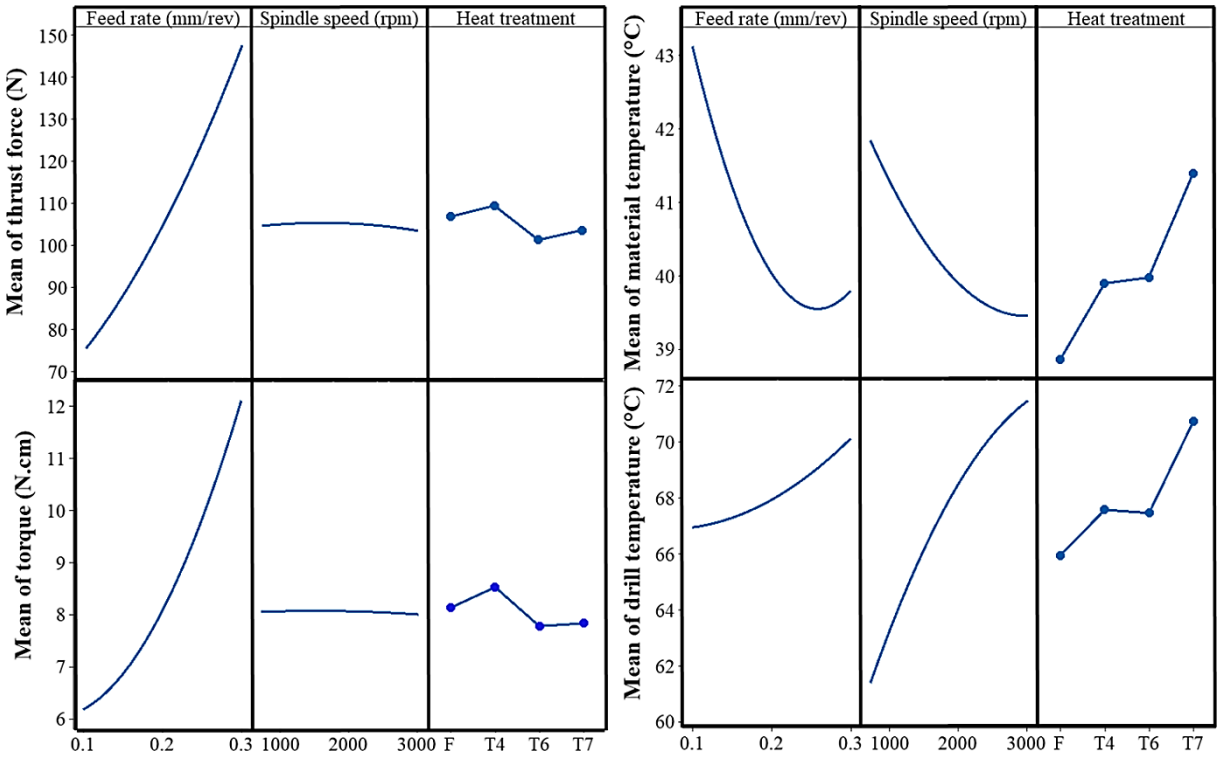


**Figure 3.** Main effect plots for thrust force, torque, material, and drill temperature.

Contour graphs obtained depending on the cutting parameters are given in Figure 4. Increasing the feed rate for each temper condition causes a progressive increase in the thrust force. On the other hand, spindle speed increase shows a pretty weak effect, which decreases $F_z$ in the T6 condition and increases in the T7 condition. $M_z$ values increased with increasing feed rate for all heat-treatment conditions. Alternatively, the weak effect of the spindle speed increase in T6 and T7 conditions was also observed for $M_z$ values. A relatively small difference in hardness values of T6 and T7 treated samples results in weak influence in $F_z$ and $M_z$. As a result, it was seen that the distributions obtained for the cutting torques and forces were compatible with each other.

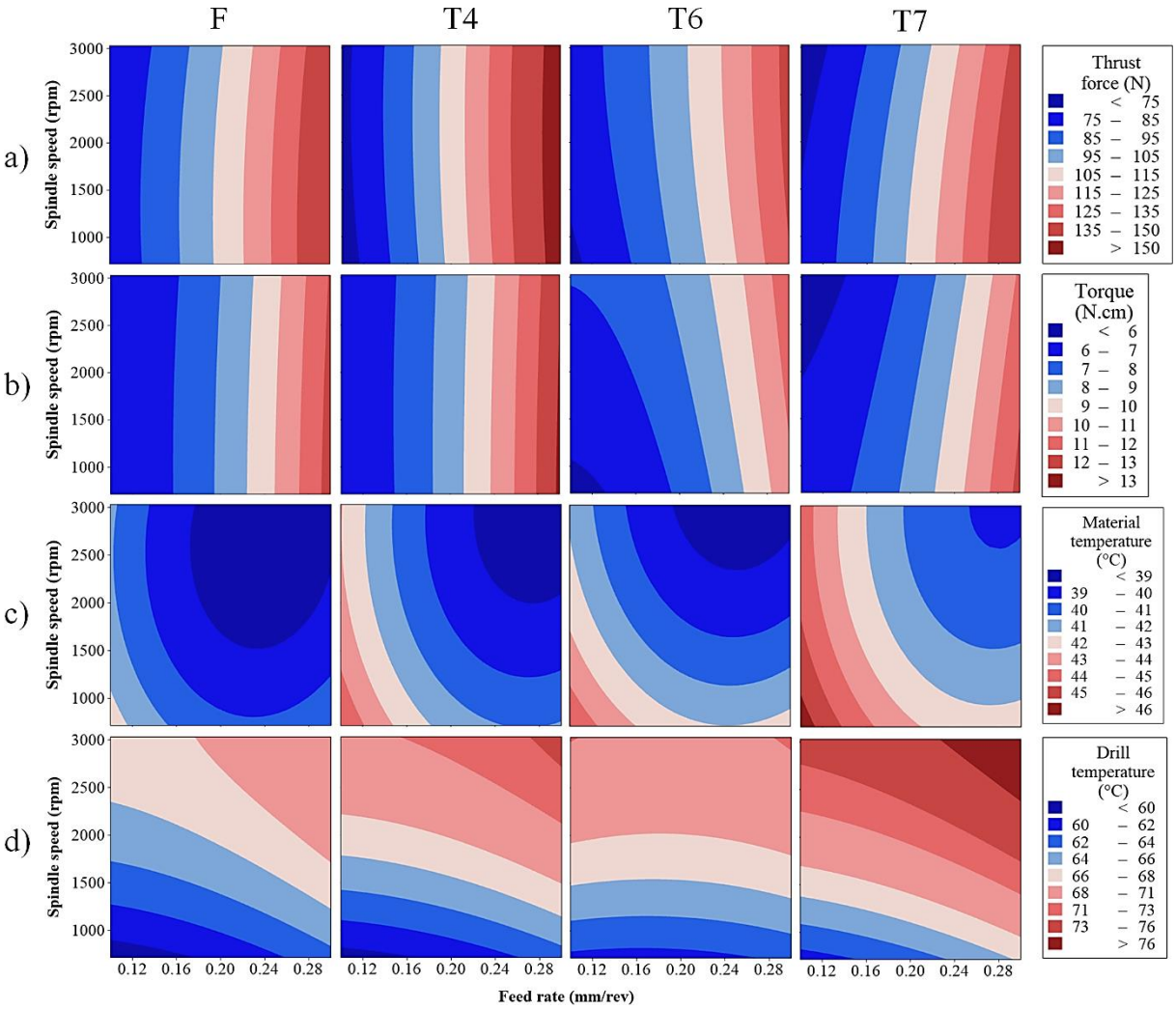


**Figure 4.** Contour plots of a) thrust force, b) torque, c) material temperature, and d) drill temperature for different cutting parameters.

### 3.2. Temperature analyses during the drilling operation

A part of research on thermal aspects of the drilling operations has concentrated on measuring the temperature of obtaining the mean temperatures in the cutting tool and the workpiece surface. These measurements provide information about the temperatures on the shear plane and the tool-chip interface, the intensity and distribution of heat sources in drilling operations. There is always heat conduction occurring within the workpiece, the chip, and the tool. The thermo-mechanical effect occurs during material removal processes as plastic deformation of the workpiece and the friction along with the tool-chip interface. Therefore, it is substantial to understand how drilling temperatures are affected by the drilling parameters. It is necessary to know the amount of heat generated in both the drill bit and the workpiece during the drilling of the samples, as well as the temperature level that occurs accordingly [37,44,45]. The temperatures arising in the drilling process of the tool and workpiece are examined in Figs. 3 and 4, depending on the different heat-treatments applied to AA7075 samples. There is an insignificant change of mean 3 °C in terms of the effects of feed rate variables on tool temperature. Spindle speed is a more effective parameter according to the analysis data on the tool temperature. The difference in spindle speed parameter selection causes an increase of up to 10 °C on the tool temperature. Among the heat-treatment types, samples in the T7 condition have a significant unfavorable effect on tool temperature. Other types of heat treatment, F, T4, and T6, give negligibly different results. As demonstrated by the thermal camera images taken

during the drilling operation in Figure 5, generated heat dissipates by the workpiece, the tool, and chips to the environment. The high thermal conductivity of the AA7075 material contributes to the rapid cooling of the specimen by providing heat dissipation.

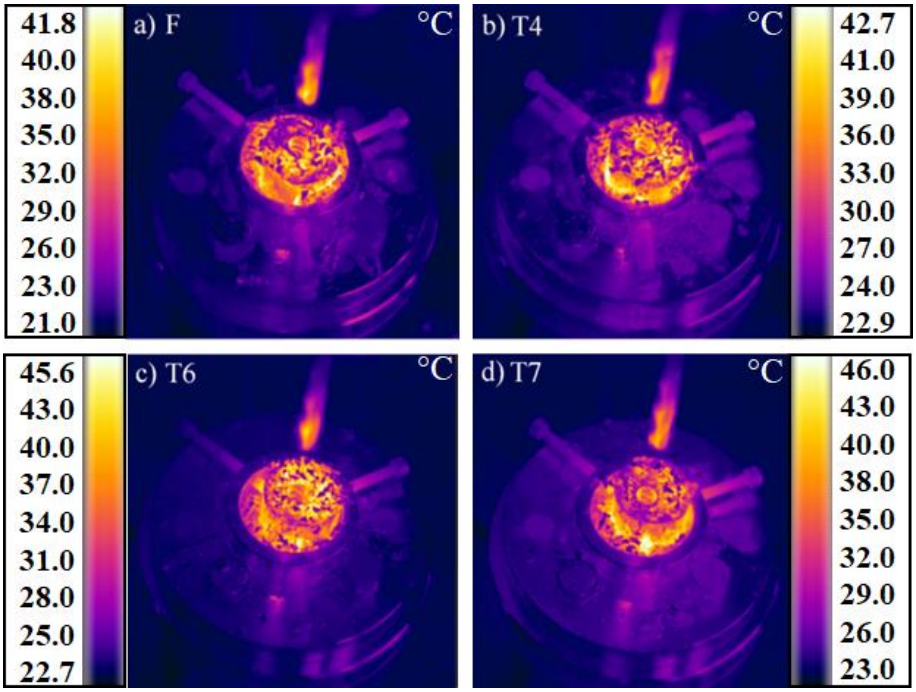


**Figure 5.** Heat generation after drilling with 0.1 feed rate and 1520 spindle speed.

Figures 3 and 4 show the occurred temperatures in the workpiece at different heat treatment conditions during the drilling process, depending on the process parameters. As a result of the increase in parametric level, both feed rate and spindle speed factors, there is a slight decrease in the temperature of the workpiece during operation. The occurred temperature in the workpiece for the AA7075-T7 heat treatment condition is higher than the other heat-treatment conditions. T4 and T6 heat-treatments gave similar results on workpiece temperature. However, the specimen in the F condition showed the lowest heating behavior during the drilling process. As a result, temperatures of the hole surface and drill bit are limitedly affected by the difference in heat-treatment type.

In Figures 4c and 4d, the workpiece and drill bit showed a maximum effect of 7 °C (39-46 °C) and 10 °C (60-76 °C) on the temperature measurement results, respectively. The heat generated in the deformation zone flows into the drill bit and the chip, and hence it should be included in the total temperature rise of the chip. In conventional drilling, most of the heat flows into the workpiece. Part of this heat is then transferred to the chip along the shear plane through convection from the workpiece. The drilling time calculations give us the actual heat transfer time in tested cases. Machining time and cutting speed for drilling are calculated with the Equations (2) and (3) given below:

$$T = \frac{L}{N.f} \tag{2}$$

$$C_s = \frac{\pi.D.N}{1000} \tag{3}$$

where $T$ is the machining time for drilling (min.), $L$ is the depth of hole (mm), $N$ is the drill speed (rpm), $f$ is the feed rate (mm/rev), $C_s$ is the cutting speed (m/min.) and $D$ is the hole diameter. Considering by drilling operation as two parametric limit values, higher and lower. Nominated conditions are as higher for 3030 rpm - 0.3 mm/rev, and as lower for 715 rpm - 0.1 mm/rev. Calculated the drilling times are 0.011 min and 0.14 min for higher and lower drilling conditions, respectively. Besides, cutting speed values are 57 m/min and 13.5 m/min for higher and lower drilling conditions, respectively. These calculations show that most of the heat conducts into the chip, as there is inadequate time for the generated heat to flow into the workpiece. Another point of view is to consider the effect of the heat generated during the drilling operation on the workpiece material. Considering the hot deformation temperature at 350 °C and semi-solid forging temperature at 500 °C for Al 7075, the drilling operation around 40 °C was interpreted as a negligible effect [46]. To summarize, the heat dissipation during drilling is transferred to the chips rather than the workpiece. This is also illustrated by the thermal images given in Figure 5. It shows that in all different cases, the drilling temperatures are taken by the chips formed during drilling. This observation will also be discussed further with the drilling model proposed in Section 3.5.

### 3.3. Chip formation and hole surface quality assessment

The ductile and soft properties of non-ferrous alloys make it difficult to drill because of the prolonged contact with the cutting edges of the tool. In machining operations, aluminum alloys tend to adhere to the cutting tool, which leads to build-up edge (BUE) and cutting tool wear [39,47]. The BUE is detrimental to surface roughness and dimensional accuracy. According to the temperature investigation, we have presented in the previous section, there isn't any correlation between the generated heat and thrust force or torque shown in Figure 3. Therefore, chip formation and hole surface are related primarily to the microstructure and properties of the materials compared to generated heat. In this study, since the aluminum alloy composition does not change, two opposite phenomena can dominate the machinability due to the structural differences caused by different heat treatments. The first fact is that the amount and size of the hard secondary phase in the structure are effective on the abrasive character of the alloy during processing. The second fact is that stacked cutting edge created by adhering to the workpiece makes chip formation and evacuation difficult that resulting in a detrimental effect on hole geometry and roughness. Which of these two phenomena will be prominent will vary depending on whether the structure originating from heat treatment has a hard phase or a soft adhesive phase. Intermetallic particles as secondary hard phase can be set in solid solution, grain structure, and dislocations. Forming of the particles as fine strengthening, dispersoid, and constituent role in AA7075 are all changed by the heat-treatment types.

Figure 6 shows OM images along the drilled holes and SEM images of the hole entry & exit, and a set of images presenting after operation condition of the drill bits for each heat-treatment condition. Figure 6a shows the hole inner surface and tool wear for the 7075-0 condition. On the drilled hole entrance and exit examination, the hole gets wider along with the drilling continues. The reason for hole geometry deterioration and the dense deposits of metal adhered on the tool is the adhesion behavior of the soft character of the 7075-0 structure during processing. The hole geometry is quite distorted, and undesirable compared to other conditions. Moreover, the intermetallic dissolved in the microstructure deformed the inner surface of the hole during cutting due to its brittle and fragile structure. This case indicates that condition 0 is not suitable for drilling processes. Furthermore, the thrust force was approximately 102 N in this condition. This value is about %25 higher than other temper conditions. Figure 6b shows deep incision marks in the F condition sample, even at the entrance 0.1 mm/rev. These deep traces have reached half the length of the hole. The entry diameter of the drilled hole is larger.

It decreases continuously up to the exit and reaches the minimum. The high hardness and brittle character of the F condition are the most likely reason for these defects. According to the images of the T4 condition in Figure 6c, there is a notable improvement in hole geometry and BUE compared to the findings in the 0 condition. We can list these improvements as follows, reduction in deep groove marks at the entry of the hole from OM image, reduction of dimensional difference in hole entry & exit, reduction of the amount of adhered residue on the drill bit cutting edge according to SEM images. The listed improvements are each even more pronounced in T6 heat-treatment sample results in Figure 6d. In Figure 6e, entry grooves and accumulation of workpiece material against the rake face in the post-processing images of the T7 heat-treated samples were more damaging than the T6 sample. AA7075 has four types of intermetallic compounds as secondary phases. SEM images in Figure 1 show the secondary phase distribution for each specimen. The T6 condition exhibits the finer and more homogeneous η-phases than the T7 sample. Besides, the microstructures of all heat-treatment conditions contain relatively fine AlMnFeSi and coarse $Al_2CuMg$, $Al_7Cu_2Fe$ precipitates originating from the residual Cu, Fe, and Si element. Soaking time and annealing temperature, which are heat-treatment variables, are the main factors in microstructure formation. Reportedly, annealing applications reduce yield strength and improve tensile elongation compared to as-received AA7075 materials. According to the knowledge obtained from previous studies, fine secondary particles do not show deformation in the tensile test and have limited influences on the overall structure in terms of deformation mechanism. It has also been reported that lattice turns are limited nearby the thin secondary phases. In contrast, coarse secondary particles deformed and showed a fracture [34,48]. Grains with coarse secondary particles would exhibit an easy slip system and transformed strain through the slip bands, which promote deep incision marks and sticky BUE formation in the F and T6 condition samples. During the cutting process, the coarse secondary particles underwent tear and separation.

When the SEM images for tool wear are examined, in all the wear micrographs except the drill bit wear given in Figure 6d, an intense BUE is noticeable, especially on the cutting edges. When the wear mechanism in Figure 6d is examined in more detail, it is seen that the BUE is concentrated towards the drill bit rather than the cutting edges. Moreover, for the F temper condition given in Figure 6b, it is understood that the BUE density is similar to each other at the cutting edge and the drill bit. In Figures 6a, 6c and 6e, there is intense adhesive wear on both the drill bit and the cutting edges. According to these observations, it turns out that the cutting quality of the tested aluminum alloys in the drilling processes is related to the applied heat treatments. Adhesive wear is more dominant for other heat treatments that show more ductile characteristics than T6 temper properties. This result is also compatible with the thrust force results.

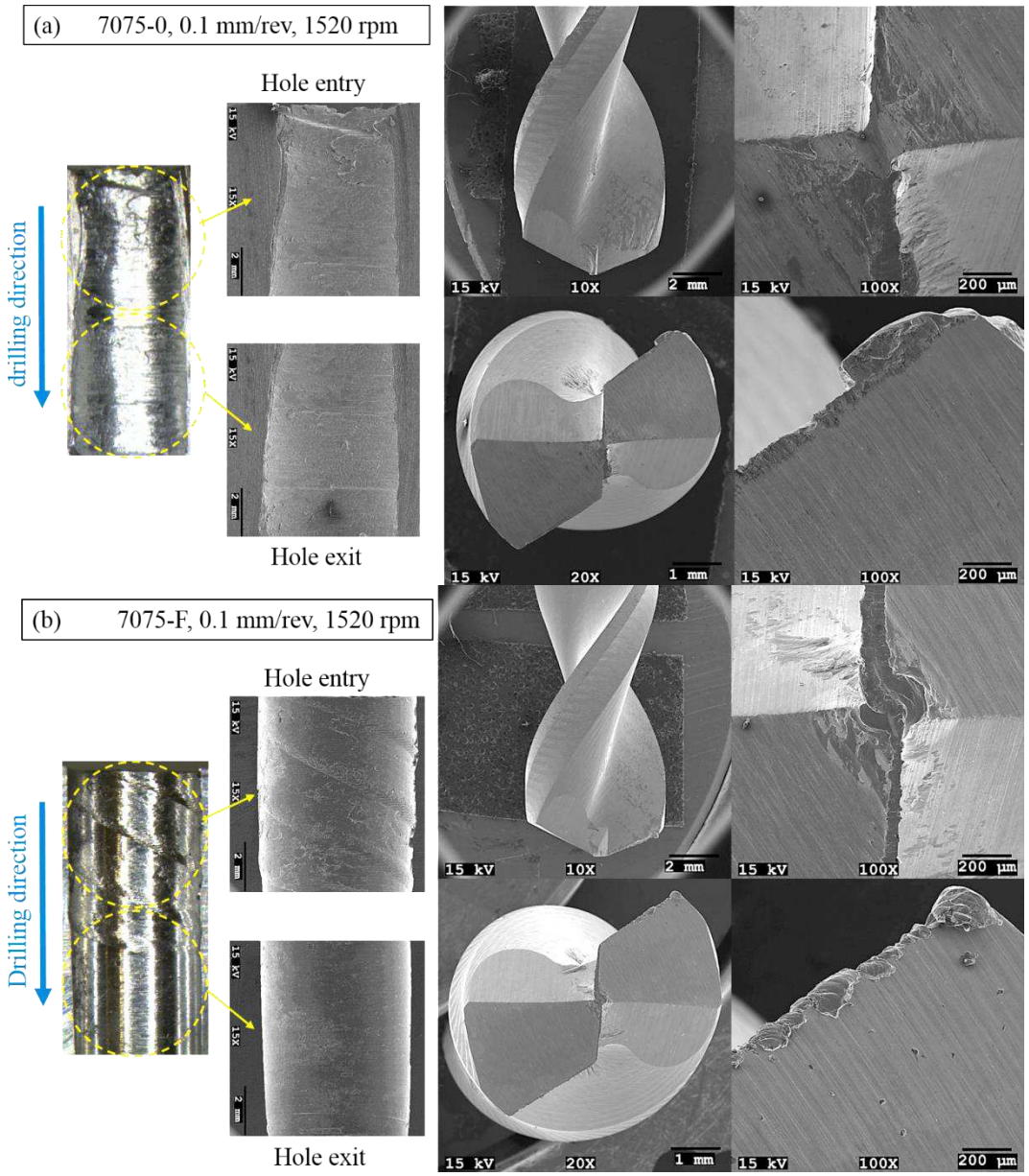
(a) 7075-0, 0.1 mm/rev, 1520 rpm
Hole entry
drilling direction
Hole exit
15 kV 10X 2 mm
15 kV 100X 200 µm
15 kV 20X 1 mm
15 kV 100X 200 µm
(b) 7075-F, 0.1 mm/rev, 1520 rpm
Hole entry
Drilling direction
Hole exit
15 kV 10X 2 mm
15 kV 100X 200 µm
15 kV 20X 1 mm
15 kV 100X 200 µm

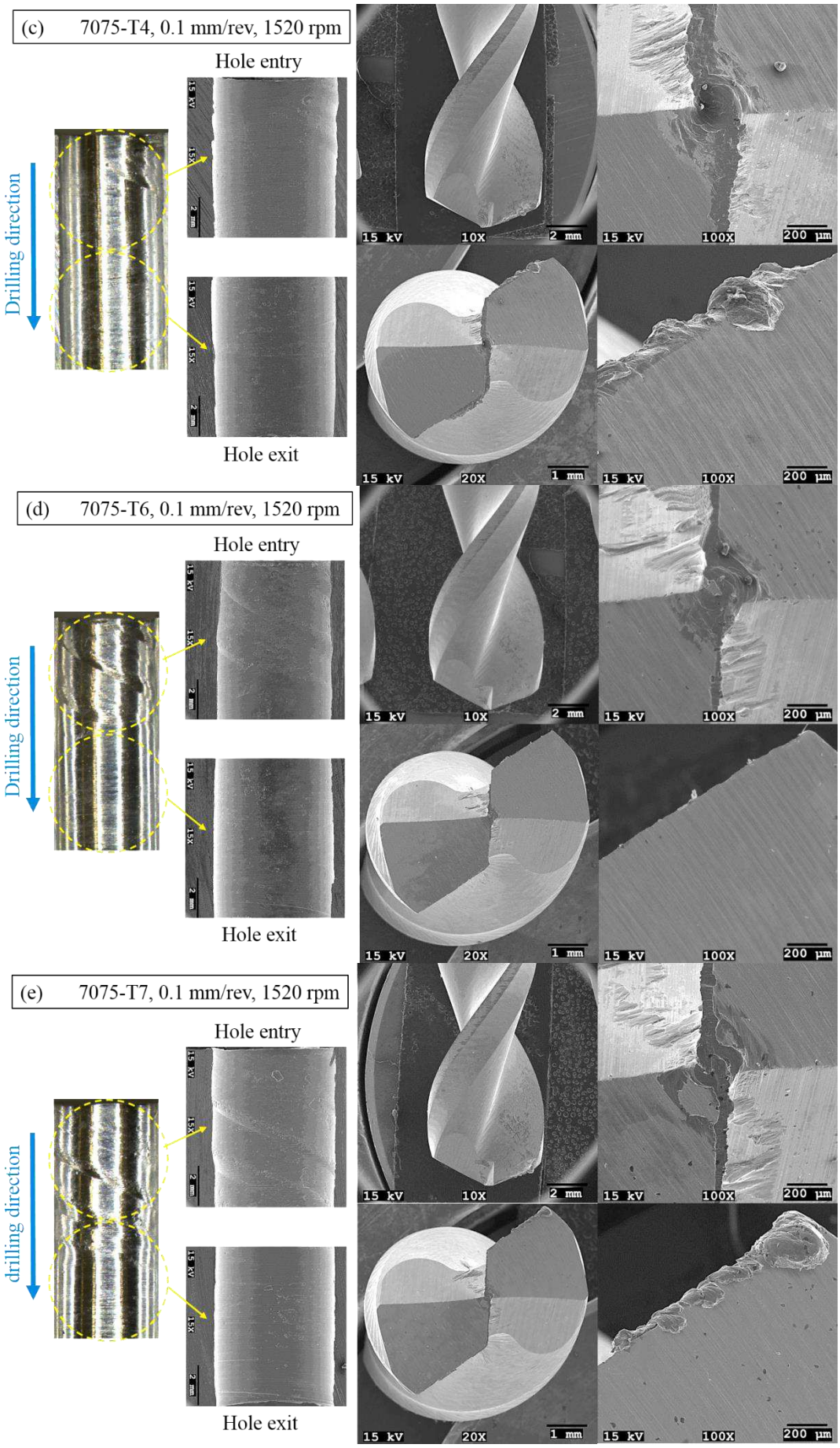
(c) 7075-T4, 0.1 mm/rev, 1520 rpm
Hole entry
Drilling direction
Hole exit
(d) 7075-T6, 0.1 mm/rev, 1520 rpm
Hole entry
Drilling direction
Hole exit
(e) 7075-T7, 0.1 mm/rev, 1520 rpm
Hole entry
drilling direction
Hole exit
15 kV 10X 2 mm
15 kV 100X 200 µm
15 kV 20X 1 mm
15 kV 100X 200 µm

**Figure 6.** A set of selected micrographs for evaluating the BUE and hole formations.

In Figure 7, different chip formations obtained in experiments conducted under the same cutting parameters (0.1 mm/rev, 1520 rpm) are presented. While deformed chip morphology occurs in Figure 7a, there are relatively fewer differences among other chip structures. The lower strength, hardness, and high ductility properties of the AA7075-0 sample made the chip flow irregular during drilling. The material that needs to be removed in the form of chips tends to stick to the drill rather than be thrown out, and the chip structure quickly deteriorates. In addition, coarse intermetallic in the microstructure provided fragility during cutting and negatively affected the plastic deformation mechanism in chip formation. As a result, the uneven chip flow deforms the hole's inner surface and increases the thrust forces. Besides, the chip formations that occur in Figures 7b and 7d are in continuous form and spiral structure. Continuous chip structure occurs at lower feed rates and in the processing of relatively ductile metals such as aluminum. This chip structure adheres to the tool and causes BUE formation [36]. BUE formation is observed for each temper condition in Figure 6. Among the chip structures, the F and T6 conditions have the most desired chip form. It is thought that $MgZn_2$ precipitates, which display a finer and homogeneous distribution in the microstructure, provide an advantage during cutting. In Figure 7c, it is seen that chip formation begins in a new flat helical form before the conical spiral chip formation ends [39]. In T4 heat treatment, the chip structure can be formed in a different form, as it cannot reach the sufficient precipitate density and therefore the maximum hardness. In Figure 7e, a relatively damaged continuous spiral chip formation is seen. Because the grain structure, which became coarse due to over-aging, decreased the hardness, increased the efficiency of the secondary phases in the microstructure, and deformed the chip structure.

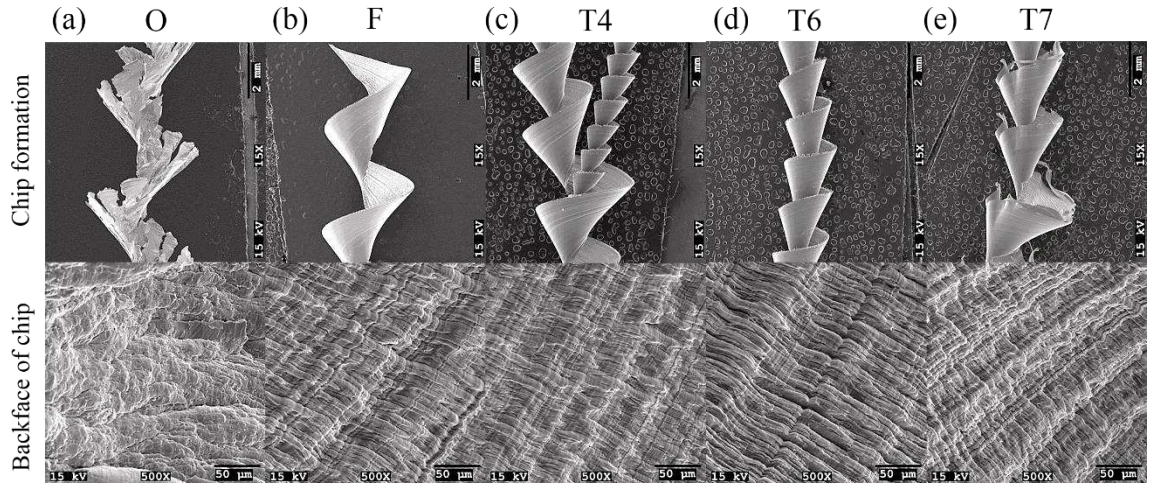


**Figure 7.** Chip formations for various heat-treatment conditions (0.1 mm/rev, 1520 rpm).

Figure 8 shows that the change in feed rate affects average surface roughness. The surface roughness measurement was separately performed at the hole entry and exit. For each temper condition, the roughness level at the hole entry is higher than the hole exits. This situation can be observed from the images of the hole inner surface given in Figure 6. The helical traces observed in the figure increased the roughness at the hole's entrance. These tracks diminished towards the hole exit because of adhesive wear at the cutting edges of the drill bit. As a result, this situation caused narrower hole exit geometry. It is also determined that the T6 temper condition has the lowest average roughness. The high strength of T6 has facilitated chip formation and flow. Thus, higher surface quality occurred. The chip structure given in Figure 7d for T6 has the desired helical and undeformed structure for drilling processes. Continuous

contact of the drill bit with the inner surface of the hole heats the drill and the workpiece, which increases the ductility and deformations of the drilled hole, resulting in higher surface roughness [49,50]. As can be seen in Figure 3, the highest cutting temperatures were obtained for the T7 temper condition. The chip structure in Figure 7e also explains occurring the roughest surface in the T7 temper condition. In general, the drilled holes become smoother with the increase of the feed rate. Considerably, feed rate in 0.3 mm/rev gives better surface roughness.

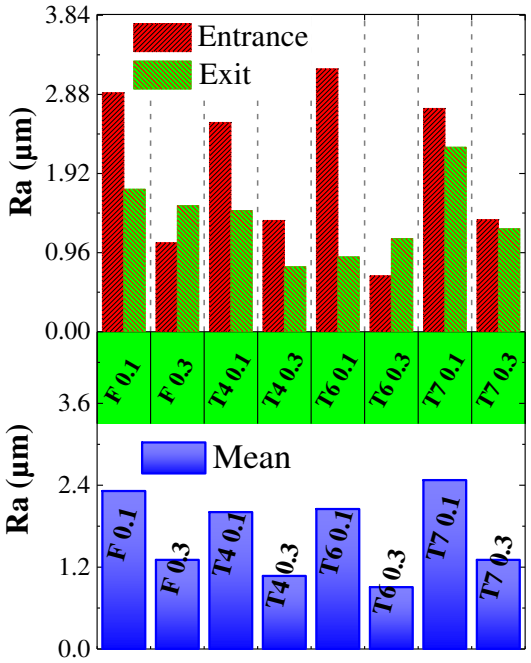


**Figure 8.** Effects of the feed rate on the surface roughness (1520 rpm).

The high thrust force is expected to negatively affect the surface roughness. However, the high ductility properties of 7075 revealed a different result than expected in this study. Increasing feed rates caused more adhesion of aluminum to the inner surface of the hole during drilling. While this increased the thrust force, it caused a decrease in the surface roughness. The roughness measurements at the hole entrance and exit separately were also made to reveal this observation. As a result, the increase in adhesive effects decreases the surface roughness.

### 3.4. Regression equations

The regression equations are given in Table 5 for thrust force, torque, material, and drill temperature were experimentally derived with the use of regression analysis and ANOVA. Here, the coefficients of linear, interaction, and quadratic terms are presented separately for each response. The ability of the regression equations to estimate the test results is expressed by the $R^2$. Predicted $R^2$ shows the ability to predict possible new observations with the obtained regression equation [51]. $R^2$ and $R^2$ (pred.) values obtained for each response are given in Table 5. Accordingly, the statistical model has a high enough ability to predict the simulation results.

**Table 5.** Empirical models of drilling operation responses.

| | | Constant | F | S | $F^2$ | $S^2$ | F.S |
|---|---|---|---|---|---|---|---|
| Thrust force (N) | F = | 59.31 | 108.8 | 0.00293 | 622 | -0.000001 | -0.00361 |
| | T4 = | 41.41 | 193.2 | 0.00487 | 622 | -0.000001 | -0.00361 |
| | T6 = | 56.74 | 59.4 | 0.00662 | 622 | -0.000001 | -0.00361 |
| | T7 = | 59.45 | 114.9 | 0.0005 | 622 | -0.000001 | -0.00361 |

| | | | | | | | |
|---|---|---|---|---|---|---|---|
| $R^2$= 96.47% $R^2$(pred.)= 95.39% | | | | | | | |
| Torque (N.cm) | F = | 5.99 | -10.62 | 0.000169 | 107.5 | 0 | -0.00067 |
| | T4 = | 5.58 | -6.85 | 0.000196 | 107.5 | 0 | -0.00067 |
| | T6 = | 6.04 | -17.89 | 0.000731 | 107.5 | 0 | -0.00067 |
| | T7 = | 6.82 | -12.92 | -0.000191 | 107.5 | 0 | -0.00067 |
| $R^2$= 89.29% $R^2$(pred.)= 85.77% | | | | | | | |
| Mat. Temp. (°C) | F = | 48.97 | -64.52 | -0.002153 | 142.92 | 0 | -0.001384 |
| | T4 = | 52.683 | -75.54 | -0.002403 | 142.92 | 0 | -0.001384 |
| | T6 = | 52.345 | -68.57 | -0.002924 | 142.92 | 0 | -0.001384 |
| | T7 = | 54.474 | -76.38 | -0.002467 | 142.92 | 0 | -0.001384 |
| $R^2$= 96.18% $R^2$(pred.)= 94.80% | | | | | | | |
| Drill. Temp. (°C) | F = | 53.38 | -1 | 0.00796 | 60.6 | -0.000001 | -0.00173 |
| | T4 = | 52.97 | -3.5 | 0.00932 | 60.6 | -0.000001 | -0.00173 |
| | T6 = | 57.39 | -18.5 | 0.0085 | 60.6 | -0.000001 | -0.00173 |
| | T7 = | 53.89 | 2.6 | 0.00987 | 60.6 | -0.000001 | -0.00173 |
| $R^2$= 93.21% $R^2$(pred.)= 90.85% | | | | | | | |

** F: Feed rate, S: Spindle Speed, D: HSS G*

### 3.5. 3D FE model of the drilling process

In this section, the drilling process of 7075 aluminum alloy is modeled using Deform 3D software. 3D computational modeling is utilized to predict chip formation, thrust force, and temperature. Based on the experimental results, the drilling process was modeled for 7075-T6 alloy and feed rate of 0.1 mm/rev and 1520 rpm, considering that T6 alloy gives the most optimum and effective results. There are modeling studies for 7075-T6 alloy using different Johnson-Cook material models in the literature [52,53]. In this study, the tabular data format containing strain, strain rate and temperature measurements with a larger scale measured separately was used. Tabular data format in the Deform 3D library was selected to define the mechanical and thermal properties of AA7075-T6:

$$\bar{\sigma} = (\bar{\varepsilon}, \dot{\bar{\varepsilon}}, T) \tag{4}$$

where $\bar{\sigma}$ is flow stress, $\bar{\varepsilon}$ is effective plastic strain, $\dot{\bar{\varepsilon}}$ is effective strain rate, and $T$ is temperature. This model is suitable for the drilling process as it defines the flow behavior as a function of strain, strain rate, and temperature. Other mechanical and thermal properties used in modeling are given in Table 6. The logarithmic interpolation method was chosen as the interpolation method. The implicit Lagrangian computational routine was used to simulate the drilling process and the distorted elements of the mesh with continuous adaptive remeshing [54]. The workpiece and drill were defined as a plastic and rigid body, respectively [55]. The frictional condition was defined as the constant shear friction factor, m = 0.7, between the aluminum workpiece-drill interface [53]. The workpiece has meshed into nearly $1.5 \times 10^5$ tetrahedron elements with a minimum element size of 0.03 mm and the high-density mesh was placed at the drilling zone. The tetrahedron element type can be efficiently used in plastic deformation simulations [56]. Similarly, the drill bit was discretized into $1 \times 10^4$ tetrahedron

elements with higher mesh density in the drilling contact zone. The 3D FE model of the drilling process is shown in Figure 9.

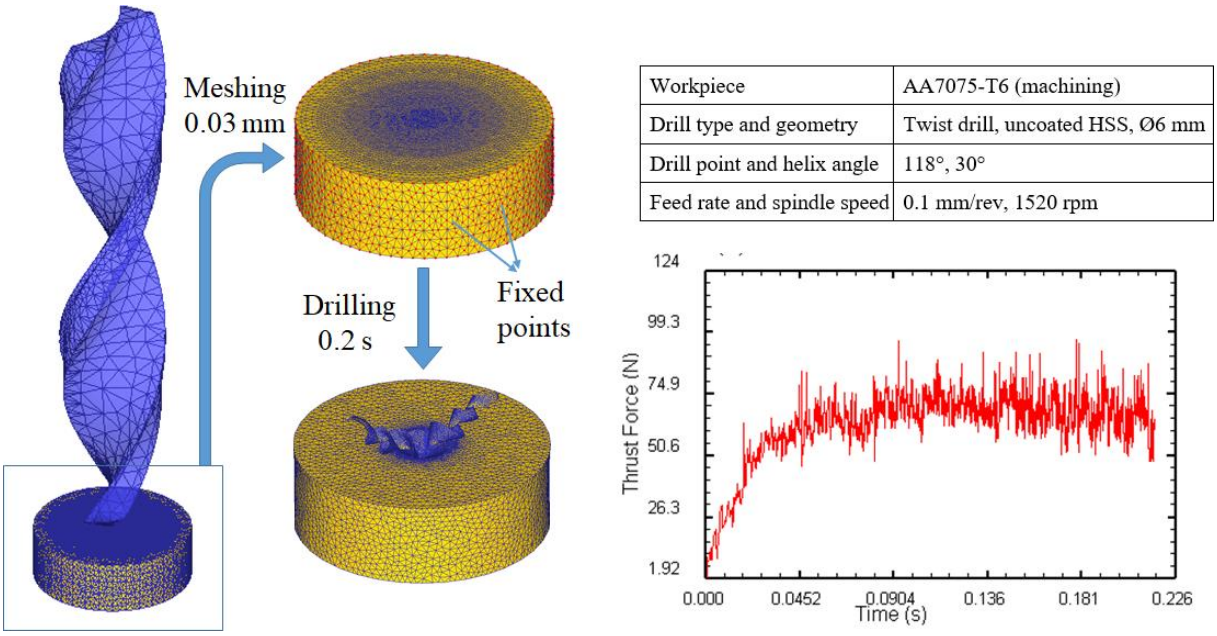


**Figure 9.** 3D FE model of drilling procedure and thrust force graph.

The thrust force graph obtained after the simulation is also given in Figure 9. Accordingly, thrust force was found at about 71.62 N. This value predicts the experimental thrust force data under the same parameters with an error of 4.62%, which is an insignificant difference. Consequently, it was observed that the developed 3D model for the drilling process is consistent with the experimental results.

**Table 6.** Mechanical and thermal properties of workpiece used in FE simulations.

| Properties | AA7075-T6 |
|---|---|
| Thermal conductivity, (N $sec^{-1}$ $°C^{-1}$) | 180.175 |
| Heat capacity, (N $mm^{-2}$ $°C^{-1}$) | 2.43369 |
| Thermal expansion coefficient, ($°C^{-1}$) | 2.2E-05 |
| Young's modulus, (GPa) | 68.9 |
| Poisson's ratio | 0.3 |

Figure 10 shows the temperature, effective stress and effective strain distributions occurring on the workpiece during drilling. Accordingly, the maximum effective strain and stress values were found to be ~ 16 (mm/mm) and ~ 790 MPa, respectively. After the regular chip flow started, the maximum stress and strain values have remained at these values throughout the simulation until the chip formation reached the conical structure. Similarly, the temperature in the contact zone was found to be about 40-45 °C. In Figure 11, the temperature change graph of the P1 point selected from the center of the workpiece is given during the simulation. Accordingly, the temperature increase of the P1 point has continued until about 50-55 °C and then a decreasing trend has begun. It is seen that the heat generated during cutting is removed from the workpiece by chip. In addition, it is seen that the predicted temperature values are in accordance with those given in Figure 5c. In AA7075-T6 drilling, the heat generated is dissipated by the chips, as exhibited in Figure 5c. The temperature distribution given in Fig. 11 is consistent with this finding. The cutting temperature in the drill-material contact area is approximately 40 °C, while the chip temperature rises to 55 °C.

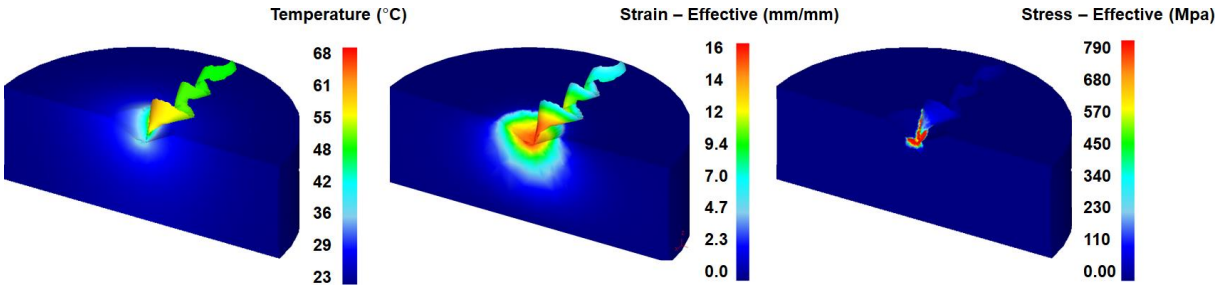


**Figure 10**. Predicted temperature, strain and stress distributions in the chip and workpiece (AA7075-T6, 0.1 mm/rev, 1520 rpm)

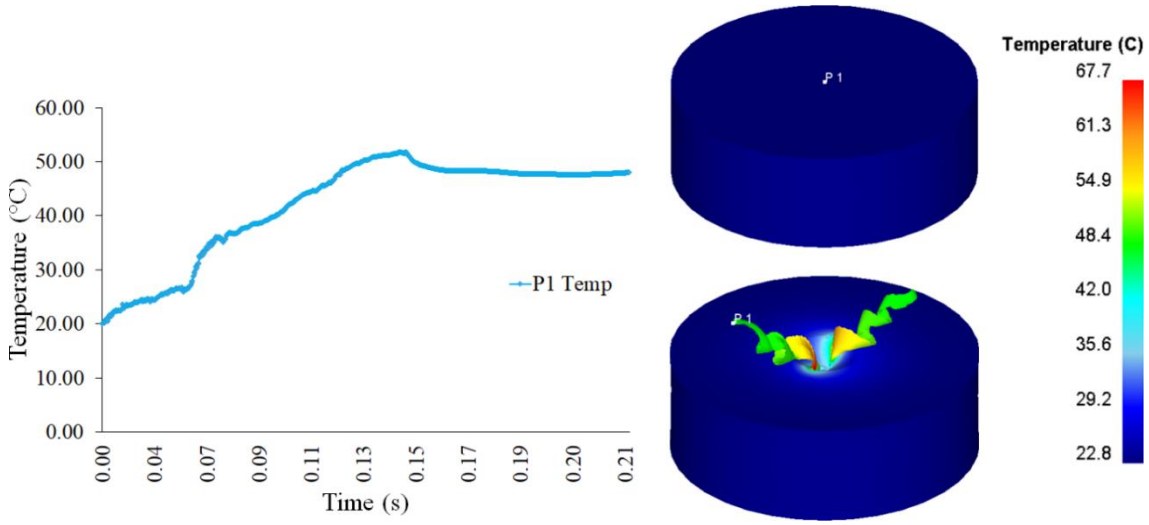


**Figure 11.** Predicted temperature distribution for the P1 point.

The thrust force and temperature distribution obtained in the simulation so far are compatible with the experimental data. These data are decisive for parameters affecting chip formation. This conformity is expected to be in harmony with the chip structure during drilling. In Figure 12, chip structures obtained both in experimental and simulation are given. At first glance, it is striking that the chip structure formed in the simulation is almost the same as that obtained in the experiment. One of the parameters used to compare chip formations is chip thickness [53,57]. The chip thicknesses obtained in the experiment were measured using an OM. On the chip thicknesses comparing, the experimental results are in perfect agreement with the simulation results. As a result, the 3D model developed for AA7075-T6 is consistent in terms of temperature, force, and chip structures.

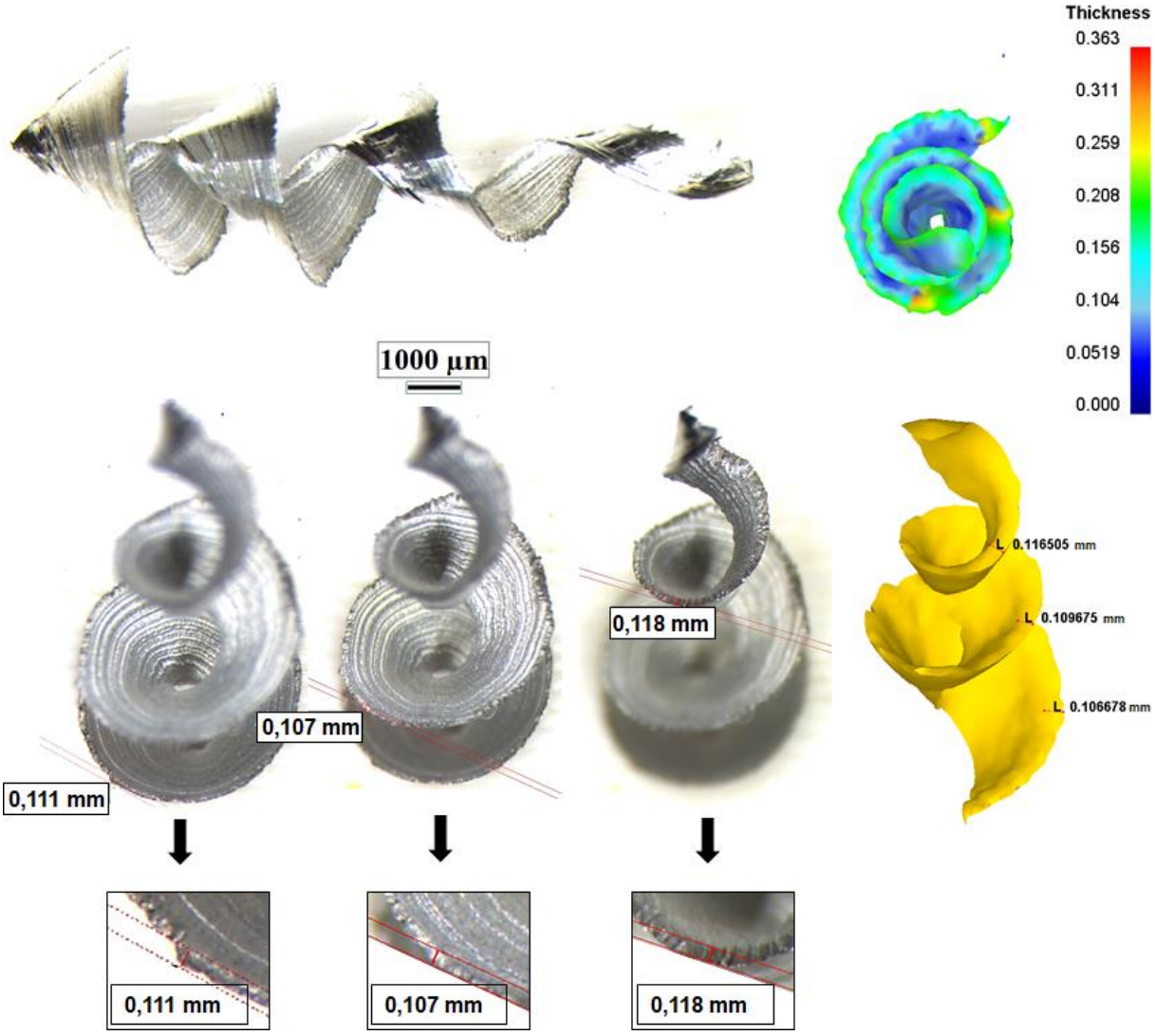


**Figure 12.** Comparison of chip formation obtained in simulation and experiment (AA7075-T6, 0.1 mm/rev, 1520 rpm)

## 4. Conclusions

In this work, the effect of heat-treatment features on drilling behaviors and chip formation mechanisms of AA7075 was investigated. The following conclusions can be drawn:

- For each temper condition, it is observed that the thrust force and torque increased with the increase of the feed rate, while the effect of the spindle speed was quite limited.
- Temper conditions put on a negligible effect on workpiece temperature during the drilling operation owing to the high thermal conductivity of the AA7075 material. In addition, the heat is removed by the chips formed during drilling.
- Chip formation and hole surface quality are related to the microstructure rather than heat generation. It is observed that the most desired chip structure was obtained by T6 heat treatment.
- The T6 condition samples resulted in deep incision marks up to half the hole length. However, it is observed that it has the lowest surface roughness since it has the lowest ductility. The T7 temper condition revealed entry grooves and accumulation against the rake face and exhibited more damaging character than the T6 samples.

- Chip formation of 0 condition sample tends to stick to the drill and deformed form. The T7 sample results in a damaged continuous spiral form, while the F and T6 conditions have the most desirable chip formation.
- There is good agreement between the experimental and numerical analysis for chip formation, thrust force, and temperature distribution. Chip formations are very similar to each other.

## Acknowledgment

The authors thank the Advanced Material Laboratory at Kocaeli University Technopark for supporting our experiments. This study was supported by Kocaeli University Scientific Research Projects Coordination Unit. Project Number: FHD-2020-1579.

## References

[1] Das D, Prasanna Sahoo B, Bansal S, Mishra P. Experimental investigation on material removal rate and chip forms during turning T6 tempered Al 7075 alloy. Mater Today Proc 2018;5:3250–6. https://doi.org/10.1016/j.matpr.2017.11.566.

[2] Gong S-H, Lee J-Y, Kim Y-J. Atom-Probe Tomographic and Electron Microscopic Analyses of a High Strength 7075-T4 Aluminum Alloy. J Nanosci Nanotechnol 2019;19:4182–7. https://doi.org/10.1166/jnn.2019.16143.

[3] Schnatterer C, Zander D. Influence of heat treatments on the stress corrosion cracking susceptibility of 7075 aluminum wires in NaCl solutions. Mater Corros 2016;67:1164–72. https://doi.org/10.1002/maco.201608978.

[4] Köklü U. Influence of the process parameters and the mechanical properties of aluminum alloys on the burr height and the surface roughness in dry drilling. Mater Tehnol 2012;46:103–8.

[5] Kao JY, Hsu CY, Tsao CC. Experimental study of inverted drilling Al-7075 alloy. Int J Adv Manuf Technol 2019;102:3519–29. https://doi.org/10.1007/s00170-019-03416-8.

[6] Yarar E, Erturk AT, Karabay S. Dynamic Finite Element Analysis on Single Impact Plastic Deformation Behavior Induced by SMAT Process in 7075-T6 Aluminum Alloy. Met Mater Int 2021;27:2600–13. https://doi.org/10.1007/s12540-020-00951-y.

[7] Jiang F, Zurob HS, Purdy GR, Zhang H. Characterizing precipitate evolution of an Al-Zn-Mg-Cu-based commercial alloy during artificial aging and non-isothermal heat treatments by in situ electrical resistivity monitoring. Mater Charact 2016;117:47–56. https://doi.org/10.1016/j.matchar.2016.04.014.

[8] Wenfeng D, Jiuhua X, Zhenzhen C, Honghua S, Yucan F. Grindability and surface integrity of cast nickel-based superalloy in creep feed grinding with brazed CBN abrasive wheels. Chinese J Aeronaut 2010;23:501–10. https://doi.org/10.1016/S1000-9361(09)60247-8.

[9] Bahçe E, Özdemir B. Investigation of the burr formation during the drilling of free-form surfaces in al 7075 alloy. J Mater Res Technol 2019;8:4198–208. https://doi.org/10.1016/j.jmrt.2019.07.028.

[10] Coldwell HL, Dewes RC, Aspinwall DK, Renevier NM, Teer DG. The use of soft/lubricating coatings when dry drilling BS L168 aluminium alloy. Surf Coatings Technol 2004;177–178:716–26. https://doi.org/10.1016/j.surfcoat.2003.08.012.

[11] Cao Y, Zhu Y, Ding W, Qiu Y, Wang L, Xu J. Vibration coupling effects and machining behavior of ultrasonic vibration plate device for creep-feed grinding of Inconel 718 nickel-based superalloy. Chinese J Aeronaut 2022;35:332–45. https://doi.org/10.1016/j.cja.2020.12.039.

[12] Miao Q, Ding W, Xu J, Cao L, Wang H, Yin Z, et al. Creep feed grinding induced

gradient microstructures in the superficial layer of turbine blade root of single crystal nickel-based superalloy. Int J Extrem Manuf 2021;3. https://doi.org/10.1088/2631-7990/ac1e05.
[13] Ding W, Dai C, Yu T, Xu J, Fu Y. Grinding performance of textured monolayer CBN wheels: Undeformed chip thickness nonuniformity modeling and ground surface topography prediction. Int J Mach Tools Manuf 2017;122:66–80. https://doi.org/10.1016/j.ijmachtools.2017.05.006.
[14] Sedighi M, Nasrollahi M, Joudaki J. Surface integrity in broaching of AA 7075-T651 aluminum alloys. Mach Sci Technol 2019;23:79–94. https://doi.org/10.1080/10910344.2018.1466329.
[15] Sivarao I, Castilo WJG, Tajul AA. Surface roughness prediction in deep drilling by fuzzy expert system. Int J Mech Mechatronics Eng 2009;9:331–5.
[16] Sofuoğlu MA, Arapoğlu RA, Orak S. Multi Objective Optimization of Turning Operation Using Hybrid Decision Making Analysis. ANADOLU Univ J Sci Technol A - Appl Sci Eng 2017:1–1. https://doi.org/10.18038/aubtda.287801.
[17] Arapoğlu RA, Sofuoğlu MA, Orak S. An ANN-Based Method to Predict Surface Roughness in Turning Operations. Arab J Sci Eng 2017;42:1929–40. https://doi.org/10.1007/s13369-016-2385-y.
[18] Orak S, Arapoğlu RA, Sofuoğlu MA. Development of an ANN-based decision-making method for determining optimum parameters in turning operation. Soft Comput 2018;22:6157–70. https://doi.org/10.1007/s00500-017-2682-8.
[19] Gök F, Orak S, Sofuoğlu MA. The effect of cutting tool material on chatter vibrations and statistical optimization in turning operations. Soft Comput 2020;24:17319–31. https://doi.org/10.1007/s00500-020-05022-3.
[20] Çakiroğlu R, Acir A. Optimization of cutting parameters on drill bit temperature in drilling by Taguchi method. Meas J Int Meas Confed 2013;46:3525–31. https://doi.org/10.1016/j.measurement.2013.06.046.
[21] Rajeswari B, Amirthagadeswaran KS. Experimental investigation of machinability characteristics and multi-response optimization of end milling in aluminium composites using RSM based grey relational analysis. Meas J Int Meas Confed 2017;105:78–86. https://doi.org/10.1016/j.measurement.2017.04.014.
[22] Mondal N, Mandal S, Mandal MC. FPA based optimization of drilling burr using regression analysis and ANN model. Meas J Int Meas Confed 2020;152:107327. https://doi.org/10.1016/j.measurement.2019.107327.
[23] LI J feng, PENG Z wei, LI C xing, JIA Z qiang, CHEN W jing, ZHENG Z qiao. Mechanical properties, corrosion behaviors and microstructures of 7075 aluminium alloy with various aging treatments. Trans Nonferrous Met Soc China (English Ed 2008;18:755–62. https://doi.org/10.1016/S1003-6326(08)60130-2.
[24] Atkinson H V., Burke K, Vaneetveld G. Recrystallisation in the semi-solid state in 7075 aluminium alloy. Mater Sci Eng A 2008;490:266–76. https://doi.org/10.1016/j.msea.2008.01.057.
[25] Vatansever F, Erturk AT, Feyzullahoglu E. Effect of ultrasonic melt treatment on the tribological behavior of 7075 aluminum alloy. Mater Test 2020;62:1243–50. https://doi.org/10.3139/120.111610.
[26] Ghalehbandi SM, Fallahi Arezoodar A, Hosseini-Toudeshky H. Influence of aging on mechanical properties of equal channel angular pressed aluminum alloy 7075. Proc Inst Mech Eng Part B J Eng Manuf 2017;231:1803–11. https://doi.org/10.1177/0954405415612370.
[27] Kilickap E. Modeling and optimization of burr height in drilling of Al-7075 using Taguchi method and response surface methodology. Int J Adv Manuf Technol

2010;49:911–23. https://doi.org/10.1007/s00170-009-2469-x.
[28] Gu R, Liu Q, Chen S, Wang W, Wei X. Study on High-Temperature Mechanical Properties and Forming Limit Diagram of 7075 Aluminum Alloy Sheet in Hot Stamping. J Mater Eng Perform 2019;28:7259–72. https://doi.org/10.1007/s11665-019-04436-x.
[29] John, G. K. Introduction to aluminum alloys and tempers. 2000.
[30] Zang JX, Zhang K, Dai SL. Precipitation behavior and properties of a new high strength Al-Zn-Mg-Cu alloy. Trans Nonferrous Met Soc China (English Ed 2012;22:2638–44. https://doi.org/10.1016/S1003-6326(11)61511-2.
[31] Isadare AD, Aremo B, Adeoye MO, Olawale OJ, Shittu MD. Effect of heat treatment on some mechanical properties of 7075 Aluminium alloy. Mater Res 2013;16:190–4. https://doi.org/10.1590/S1516-14392012005000167.
[32] Rometsch PA, Zhang Y, Knight S. Heat treatment of 7xxx series aluminium alloys - Some recent developments. Trans Nonferrous Met Soc China (English Ed 2014;24:2003–17. https://doi.org/10.1016/S1003-6326(14)63306-9.
[33] Guo W, Guo J, Wang J, Yang M, Li H, Wen X, et al. Evolution of precipitate microstructure during stress aging of an Al-Zn-Mg-Cu alloy. Mater Sci Eng A 2015;634:167–75. https://doi.org/10.1016/j.msea.2015.03.047.
[34] Hua L, Hu X, Han X. Microstructure evolution of annealed 7075 aluminum alloy and its influence on room-temperature plasticity. Mater Des 2020;196:109192. https://doi.org/10.1016/j.matdes.2020.109192.
[35] Koç FG, Çöl M, Çeliker T. Effect of cooling rate on microstructure, mechanical properties and residual stress of 7075 aluminum alloy. Mater Test 2018;60:989–96. https://doi.org/10.3139/120.111242.
[36] Aamir M, Giasin K, Tolouei-Rad M, Vafadar A. A review: drilling performance and hole quality of aluminium alloys for aerospace applications. J Mater Res Technol 2020;9:12484–500. https://doi.org/10.1016/j.jmrt.2020.09.003.
[37] Erturk AT, Vatansever F, Yarar E, Guven EA, Sinmazcelik T. Effects of cutting temperature and process optimization in drilling of GFRP composites. J Compos Mater 2021;55:235–49. https://doi.org/10.1177/0021998320947143.
[38] Sivarao SP, Chin CW. Comparison of Statistical and Mathematical Method for determination of Tool Wear in Drilling. Strojnícky Časopis – J Mech Eng 2004;55:187–98.
[39] Yarar E, Karabay S. Investigation of the effects of ultrasonic assisted drilling on tool wear and optimization of drilling parameters. CIRP J Manuf Sci Technol 2020;31:265–80. https://doi.org/10.1016/j.cirpj.2020.06.002.
[40] Erturk AT, Vatansever F, Yarar E, Karabay S. Machining behavior of multiple layer polymer composite bearing with using different drill bits. Compos Part B Eng 2019;176:107318. https://doi.org/10.1016/j.compositesb.2019.107318.
[41] Yıldız T, Sur G. Investigation of drilling properties of AA7075/Al2O3 functionally graded materials using gray relational analysis. Proc Inst Mech Eng Part B J Eng Manuf 2021;235:1384–98. https://doi.org/10.1177/0954405421995657.
[42] Sasikumar KSK, Arulshri KP, Ponappa K, Uthayakumar M. A study on kerf characteristics of hybrid aluminium 7075 metal matrix composites machined using abrasive water jet machining technology. Proc Inst Mech Eng Part B J Eng Manuf 2018;232:690–704. https://doi.org/10.1177/0954405416654085.
[43] Sivaraos S, Kasim MS, Ali MAM, Abdullah RIR, Anand TJS. Micro-drilling of silicon wafer by industrial CO2 laser. Int J Mech Mater Eng 2015;10:2–7. https://doi.org/10.1186/s40712-015-0029-8.
[44] Dörr J, Mertens T, Engering G, Lahres M. “In-situ” temperature measurement to determine the machining potential of different tool coatings. Surf Coatings Technol

2003;174–175:389–92. https://doi.org/10.1016/S0257-8972(03)00708-4.
[45] Khajehzadeh M, Razfar MR. Theoretical modeling of tool mean temperature during ultrasonically assisted turning. Proc Inst Mech Eng Part B J Eng Manuf 2016;230:675–93. https://doi.org/10.1177/0954405414556333.
[46] Senkova S V., Senkov ON, Miracle DB. Cryogenic and elevated temperature strengths of an Al-Zn-mg-Cu alloy modified with Sc and Zr. Metall Mater Trans A Phys Metall Mater Sci 2006;37:3569–75. https://doi.org/10.1007/s11661-006-1051-5.
[47] Rouniyar AK, Shandilya P. Fabrication and experimental investigation of magnetic field assisted powder mixed electrical discharge machining on machining of aluminum 6061 alloy. Proc Inst Mech Eng Part B J Eng Manuf 2019;233:2283–91. https://doi.org/10.1177/0954405419838954.
[48] Liu C, Liu Y, Ma L, Yi J. Effects of solution treatment on microstructure and high-cycle fatigue properties of 7075 aluminum alloy. Metals (Basel) 2017;7. https://doi.org/10.3390/met7060193.
[49] Al-Tameemi HA, Al-Dulaimi T, Awe MO, Sharma S, Pimenov DY, Koklu U, et al. Evaluation of cutting-tool coating on the surface roughness and hole dimensional tolerances during drilling of Al6061-T651 alloy. Materials (Basel) 2021;14. https://doi.org/10.3390/ma14071783.
[50] Giasin K, Hodzic A, Phadnis V, Ayvar-Soberanis S. Assessment of cutting forces and hole quality in drilling Al2024 aluminium alloy: experimental and finite element study. Int J Adv Manuf Technol 2016;87:2041–61. https://doi.org/10.1007/s00170-016-8563-y.
[51] Ramya Devi G, Palanikumar K. Analysis on drilling of woven glass fibre reinforced aluminium sandwich laminates. J Mater Res Technol 2019;8:1024–35. https://doi.org/10.1016/j.jmrt.2018.06.021.
[52] Luo H, Fu J, Wu T, Chen N, Li H. Numerical Simulation and Experimental Study on the Drilling Process of 7075-t6 Aerospace Aluminum Alloy 2021.
[53] Ucun İ. 3D finite element modelling of drilling process of Al7075-T6 alloy and experimental validation. J Mech Sci Technol 2016;30:1843–50. https://doi.org/10.1007/s12206-016-0341-0.
[54] Özel T. Computational modelling of 3D turning: Influence of edge micro-geometry on forces, stresses, friction and tool wear in PcBN tooling. J Mater Process Technol 2009;209:5167–77. https://doi.org/10.1016/j.jmatprotec.2009.03.002.
[55] Paktinat H, Amini S. Ultrasonic assistance in drilling: FEM analysis and experimental approaches. Int J Adv Manuf Technol 2017;92:2653–65. https://doi.org/10.1007/s00170-017-0285-2.
[56] Thepsonthi T, Özel T. 3-D finite element process simulation of micro-end milling Ti-6Al-4V titanium alloy: Experimental validations on chip flow and tool wear. J Mater Process Technol 2015;221:128–45. https://doi.org/10.1016/j.jmatprotec.2015.02.019.
[57] Lotfi M, Amini S. Experimental and numerical study of ultrasonically-assisted drilling. Ultrasonics 2017;75:185–93. https://doi.org/10.1016/j.ultras.2016.11.009.

# Supplementary Files

This is a list of supplementary files associated with this preprint. Click to download.

- SUPPLEMENTARYDATA.docx